3D Quantitative Analysis of Graphite Morphology in Ductile Cast Iron by X-ray Microtomography

YAJUN YIN, ZHIXIN TU, JIANXIN ZHOU, DONGQIAO ZHANG, MIN WANG, ZHAO GUO, CHANGCHANG LIU, and XIANG CHEN

In this article, X-ray microtomography and color metallographic techniques have been used to perform three-dimensional quantitative characterization of graphite nodule morphology in a step-shaped ductile cast iron casting. Statistical analyses of the graphite nodule count, diameter, sphericity, and spatial distribution have been processed for three samples in detail. The results reveal that graphite nodules in ductile cast iron can be categorized into two categories. The first types are nodules located in eutectic cells (NIECs), and the other one refers to nodules located between the eutectic cells (NBECs). The NIECs possess a larger average diameter but smaller sphericity compared with the NBECs, and the sphericity decreases along with the increasing of diameter. The increasing casting thickness results in an increasing count and percentage of NBECs. In addition, most nodules are NIECs in thin walls instead of NBECs in thick walls. Nonuniform spatial distributions of graphite nodules caused by the existence of NBECs have been found to become more obvious along with the increase of cast thickness.

DOI: 10.1007/s11661-017-4130-x
© The Minerals, Metals & Materials Society and ASM International 2017

I. INTRODUCTION

DUCTILE cast iron (DCI) is an important kind of metal material that has high strength, good toughness, low cost, and impeccable castability. DCI was first introduced to manufacturing in the 1940s,[1] and it has been researched and used for more than 70 years. DCI has been widely used because of its comprehensive mechanical property and processability.[2] The mechanical properties of DCI are seriously influenced by the morphology of the graphite nodule, including count, diameter, sphericity, and spatial distribution. For instance, the sphericity, and spatial distribution of nodules affect strength and toughness. Fatigue strength is influenced by count and diameter.[3–5]

Numerous studies using a variety of methods have been conducted to investigate the graphite morphology of DCI, and of all the methods, thermal analysis is an available and effective way. Chen *et al.*[6] predicted sphericity of nodules in hypoeutectic DCI correctly by computer-aided differential thermal analysis. Zhu *et al.*[7] found that the thermal analysis results were not only microstructure (graphite morphology) sensitive but also nodulizer and trace element sensitive. Sheikhabdolhossein[8] investigated the spheroidization fading phenomenon by analyzing the cooling curves of DCI with the addition of a nodulizer under different lengths of heat preservation time. They found that the magnitude of undercooling increased and that the temperature of eutectic undercooling decreased because of the processing of fading. Some quantitative models were also established.[9–12] For example, Kapturkiewicz *et al.*[10] established a solidification mathematical model for near-eutectic, thin-wall DCI castings, and the correctness of the mathematical model was experimentally verified by comparison with characteristic points on the cooling curve and nodule count. Liquid quenching and metallography analysis, as basic approaches, still play important roles. Natxiondo *et al.*[13] researched graphite and solid fraction evolutions during solidification of DCI by liquid quenching.

The metallography can present two-dimensional (2D) morphology of graphite directly comparing with thermal analysis. Image analysis was used to evaluate nodule count, graphite diameter, and sphericity, matrix structure by Ruxanda and Stefanescu.[14] Morales-Hernández *et al.*[15] studied 2D spatial distribution and sphericity characterization of graphite nodule based on morphological tools. As research continues, study of three-dimensional (3D) morphology such as size and count appears and becomes more relevant. Basak[16] first put forward a method to characterize the 3D size distribution of a spherical second phase from 2D size distribution by using a finite difference method based on a mathematical model. Pedersen[17,18] studied nucleation

YAJUN YIN, ZHIXIN TU, JIANXIN ZHOU, DONGQIAO ZHANG, MIN WANG, ZHAO GUO, CHANGCHANG LIU, and XIANG CHEN are with the State Key Laboratory of Materials Processing and Die & Mould Technology, Huazhong University of Science and Technology, Wuhan 430074, Hubei Province, P.R. China. Contact e-mail: zhoujianxin@hust.edu.cn
Manuscript submitted December 21, 2016.
Article published online May 23, 2017

and solidification of thin-walled DCI castings by experiments and numerical simulation. The distribution of count and diameter of nodules calculated by the finite difference method revealed that there was little nucleation at the end of solidification in thin-wall DCI casting. Unfortunately, the results obtained by the finite difference method were only an approximation of real 3D size and count distribution.

With application of new methods such as X-ray tomography, focused ion beam tomography, and scanning electron microscopy, direct study of 3D graphite morphology becomes easier. Lekak *et al.*[19] analyzed graphite nodule size distribution in DCI by optical metallography and scanning electron microscopy/energy-dispersive X-ray. The results show two different types of nodule size distributions: a normal one mainly composed by monosized nodules and an abnormal one consisting of two or three different graphite size nodules. Stefanescu[20] studied the solidification of stable eutectic iron-carbon-silicon alloys including the spheroidal-to-compacted graphite transition. Morphology, such as spatial arrangement and orientation, of spheroidal graphite, compacted graphite, and flake graphite in cast iron were quantitatively characterized based on the focused ion beam tomography by Velichko.[21,22] Li *et al.*[23] introduced a fractal dimension to quantitatively analyze the irregularity of the graphite nodule in cast iron. Chuang[24] quantitatively analyzed graphite morphology in high-strength compacted cast iron by high-energy X-ray tomography, and the result showed that the compacted graphite can grow into a coral-tree-like morphology and span several hundred microns in the iron matrix.

In these studies, research on graphite morphology was confined to two dimensions, and only several graphite nodules have been qualitatively characterized in three dimensions. There are a few studies on spatial distribution and statistical analysis of a large number of graphite nodules in three dimensions. The aim of the present work is to investigate 3D graphite morphology (count, diameter, sphericity, and spatial distribution) under different cooling rates. First, a step-shaped casting is gained by the lost foam casting. The cooling curves during the process of solidification are obtained by thermocouples. Then, the 3D morphology of graphite is acquired using X-ray microtomography. Last, the count, diameter, sphericity, and spatial distribution in 3D are quantitatively analyzed by thermal analysis and color metallographic techniques.

II. RESEARCH APPROACH

A step-shaped symmetrical casting is produced by lost foam casting. On one side of the casting, K-type thermocouples are used to acquire cooling curves in the center of each step. The temperature sampling frequency is 1.5 Hz. The steps of the casting are numbered from 0 to 5 in sequence of thickness from 15 to 110 mm sequentially. The detailed casting layout and thermocouples layout are shown in Figure 1. A different thickness step results in a different cooling rate. Table I shows the chemical composition of the adopted DCI. Nodulant and inoculant are composed of RE-Mg alloy and Ba-Si-Mg alloy, respectively. The pouring temperature is 1653 K (1380 °C).

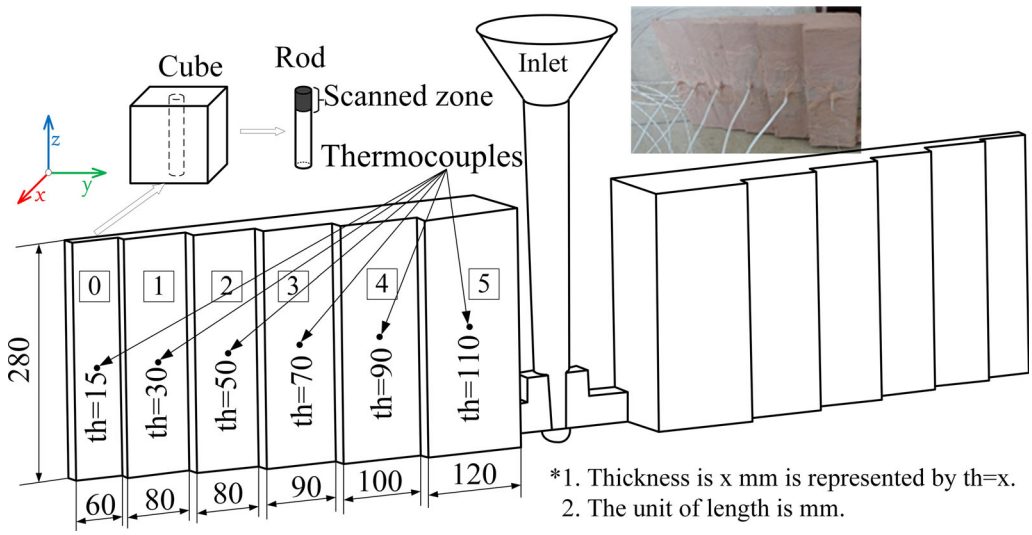

Fig. 1—Casting and thermocouple layout.

Table I. Chemical Composition of the Employed DCI (Wt Pct, CE = C + 0.28 × Si[18])

C	Si	Mn	S	P	Mg	RE	CE
3.6-3.8	2.4-2.6	≤0.40	≤0.015	≤0.06	0.06-0.08	0.02	4.27-4.53

In the current study, the steps with 15, 50, and 90 mm are chosen in consideration of the failure of temperature acquirement in 10- and 70-mm steps. First, the cubes samples with a side length of 10 mm are taken out from the center of the chosen step. Then cylindrical rods with a size of ∅2 × 10 mm are taken out from the center of every cube, as shown in Figure 1. Cylindrical rods (numbered 0, 2, and 4) are scanned by X-ray microtomography, and the scanning zone is ∅2 × 2 mm. The X-ray microtomography experiments were performed at the *Phoenix Nanotom M*. The resolution of the present experimental setup is 1 μm, which means that 1 voxel of 3D volume is equal to 1 μm^3. To obtain 3D morphology and distribution of graphite nodules in the specimens, the reconstruction and visualization of 3D volume are processed. The 3D volume data is analyzed using the *VGStudio Max*, which is the software for the analysis and visualization of industrial computed tomography data. The 2D morphology of the nodules in the rods has been obtained by color metallographic techniques. The rods have been prepared by polishing and hot alkali etching.[25,26] Etchant consists of 100-g sodium hydroxide, 8-g picric acid, and 200-mL distilled water. Samples are placed in etchant for 1.5 to 5 minutes at temperature ranging from 368 K to 373 K (95 °C to 100 °C).

To describe the solidification process better, some characteristic temperature points are defined on a cooling curve.[8] The temperature of eutectic undercooling (T_{eu}), temperature of eutectic recalescence (T_{er}), and magnitude of recalescence ($\Delta T = T_{er} - T_{eu}$) are defined. The corresponding values of temperature are illustrated in Figure 2.

As a result of the noise interference by the X-ray microtomography, the invalid scanning data obtained at the rod's edge are removed when researching the statistics phenomenon of the graphite nodules. In the present experiment, the chosen 3D volume is ∅1.6 × 1.2 mm. Moreover, the graphite nodules whose diameter is smaller than 25 μm are ignored because of the resolution of 3D volume and the interference of inclusion and microporosity. The nodules are segmented using a global threshold gray value, and the geometrical parameters (such as volume, surface area, *etc.*) of nodules are quantified by *VGStudio Max* software. The diameter of the nodules is equal to that of the circumscribed sphere. The sphericity of graphite[24] (S_G) is defined as:

$$S_G = \frac{\sqrt[3]{\pi(6V_r)^2}}{A_r}, \qquad [1]$$

where V_r (mm^3) is the volume of the nodule and A_r (mm^2) is the surface area of the nodule. In theory, the sphericity of a perfect sphere is equal to 1.0. But as a result of the algorithm for surface area calculation and the relative size of the voxel and the graphite nodules,[24] the sphericity of a perfect sphere in the present study is between 0.5 and 0.6. According to the analysis by Chuang *et al.*[27] when the diameter is larger than 25 pixels (25 μm), the underestimation of sphericity does not influence the analytical results. Nodules with various sphericities are shown in Figure 3. The nodule with a sphericity of 0.6 is quasi-spherical, and the sphericity of nodules with gap-like defects is smaller than 0.6.

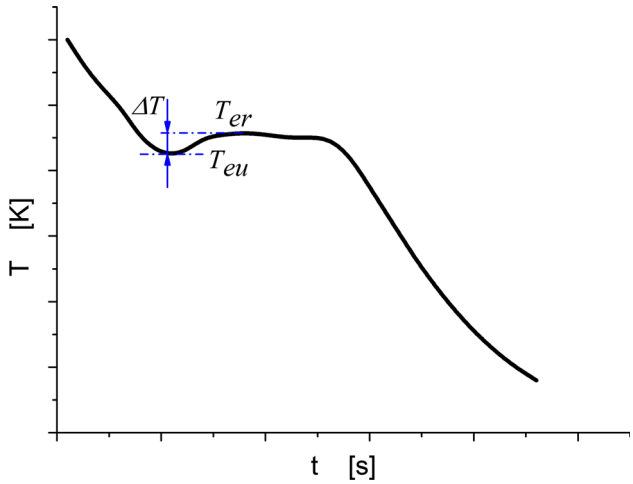

Fig. 2—Typical cooling curve and its characteristic points.

III. RESULT

A. *Cooling Curves of the Step-Shaped Iron Casting*

$T \sim t$ curves of sample 0, 2, and 4 are shown in Figure 4, and the characteristic temperature values are shown in Table II. It is obvious that the solidification time increases with thickness increasing. The values of

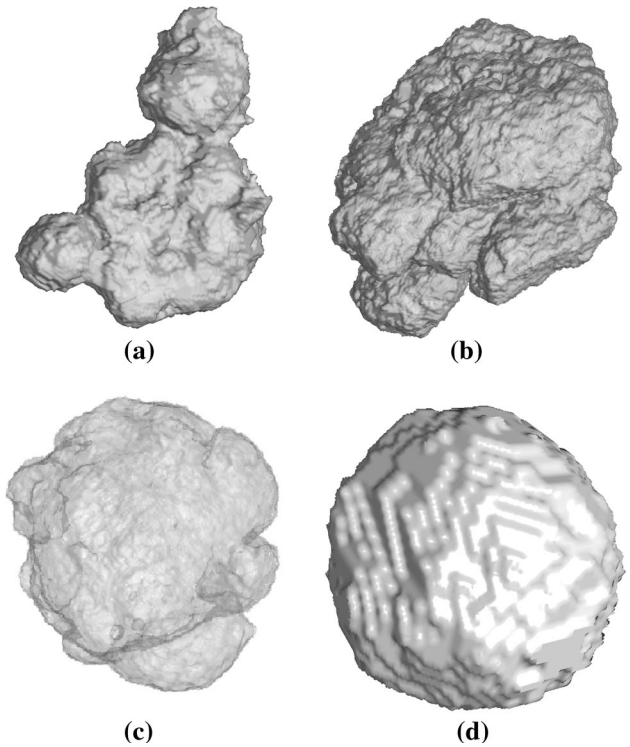

Fig. 3—Nodule sketch with different sphericity: (*a*) S_G = 0.3; (*b*) S_G = 0.4; (*c*) S_G = 0.5; and (*d*) S_G = 0.6.

T_{eu} and T_{er} increase as the step thickness increases. T_{eu} and T_{er} in sample 0 are smaller than that in samples 2 and 4 because these steps have smaller thickness. As the thickness increases, ΔT first increases and then decreases.

B. *Spatial Distributions of Graphite Nodules*

Spatial distributions of nodules in different samples are shown in Figure 5. The colored particles are graphite nodules. To show distributions of nodules within a given diameter range, only part of the nodules is colored and the other nodules are gray as shown in Figures 5(b) through (e), (g) through (j), and (l) through (o). When thickness is equal to 15 mm, all nodules are uniformly distributed in matrix microstructures, as shown in Figures 5(a) through (e). When the thickness of step increases to 40 and 90 mm, the nodules with small diameter aggregate together dramatically as shown in Figures 5(f) through (j) and (k) through (o). So the distribution distinctly partitions the volume into two regions, where the large and small nodules are distributed respectively.

The nodules with a different diameter range are uniformly distributed in sample 0 as shown in Figures 5(b) and (e). The nodules larger than 150 μm in samples 2 and 4 are also uniformly distributed in the corresponding region as shown in Figures 5(g) and (l). In samples 2 and 4, nodules gradually aggregate together as the diameter decreases. In sample 2, nodules slightly aggregate in the diameter range of 50 to 100 μm and, remarkably, in 25 to 50 μm as shown in Figures 5(i) and (j). In sample 4, nodules slightly aggregate in the diameter range of 100 to 150 μm and dramatically aggregate together in the diameter range of 25 to 100 μm as shown in Figures 5(m) through (o). By comparing nodule distributions in the same diameter range in samples 2 and 4, the aggregation level of nodules in sample 2 is lower than that in sample 4, as shown in Figures 5(i), (j), (n), and (o).

In the 3D volume of sample 0, all the nodules are almost uniformly distributed. Nevertheless, there are a few nodules with a diameter of 25 to 50 μm in sample 2 and a few nodules with a diameter of 25 to 100 μm in sample 4 locating in the region where the large nodules are distributed, as shown in Figures 5(j) and (n) through (o), respectively. Therefore, in samples 2 and 4, the larger nodules are surrounded by the small ones.

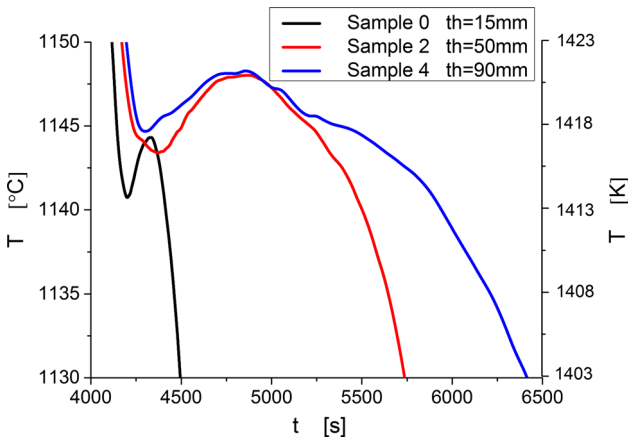

Fig. 4—Cooling curves.

Table II. Characteristic Temperature on Cooling Curves

Sample Number	T_{eu} [K(°C)]	T_{er} [K(°C)]	ΔT [K (°C)]
0	1413.7 (1140.7)	1417.5 (1144.5)	3.8
2	1416.5 (1143.5)	1421.0 (1148.0)	4.5
4	1417.3 (1144.3)	1421.3 (1148.3)	4.0

C. *Count, Diameter, Sphericity Distribution*

Total count, relationship between diameter and count, and relationship between diameter and volume are shown in Figures 6 and 7. In samples 2 and 4, all the nodules larger than 300 μm are categorized into the nodule group with a diameter range of 300 to 325 μm for convenience because the number of the nodules with a diameter larger than 325 μm is very small. The total count in sample 0 is much larger than that in samples 2 and 4. Moreover, nodule count in sample 4 is more than that in sample 2. Most nodules have a diameter smaller than 150 μm, and there are few nodules with a diameter larger than 200 μm in sample 0. In samples 2 and 4, the nodule count in every diameter interval decreases with an increase of diameter. When the count is compared between samples 2 and 4, there are more nodules with a diameter larger than 100 μm and less nodules with a diameter smaller than 100 μm in sample 2, as shown in Figure 6(d). So the nodules smaller than 100 μm account for the majority of counts in sample 4.

The relationship between the cumulative volume percentages of nodule and the nodule diameter is presented in Figure 7. The cumulative volume percentage rapidly increases, and the majority of nodule volume is contributed by the nodule larger than 50 μm in sample 0. In samples 2 and 4, the curves increase more gently and the nodules larger than 100 μm possess almost 80 pct of total nodule volume although they account for the minority of the total count.

The distribution between diameter and sphericity is shown in Figure 8. The sphericity of most nodules is larger than 0.40 in three samples. The percentage of nodules with sphericity smaller than 0.4 increases with the increase of thickness. The percentage of nodules with sphericity smaller than 0.4 are 6.5, 25.1, and 26.1 pct in samples 0, 2, and 4, respectively. And when comparing Figures 8(b) with (c), most nodules with sphericity smaller than 0.4 have a diameter larger than 150 μm in sample 2. Nevertheless, the result is opposite in sample 4.

The average sphericity in different diameter ranges is shown in Figure 8(d). There are only four values in sample 0 as a result of a lack of nodules with diameters larger than 200 μm. In all three samples, the values of average sphericity generally decrease with the increase of the nodule diameter. The average sphericity in sample 2 is larger than that in sample 4 when the diameter is

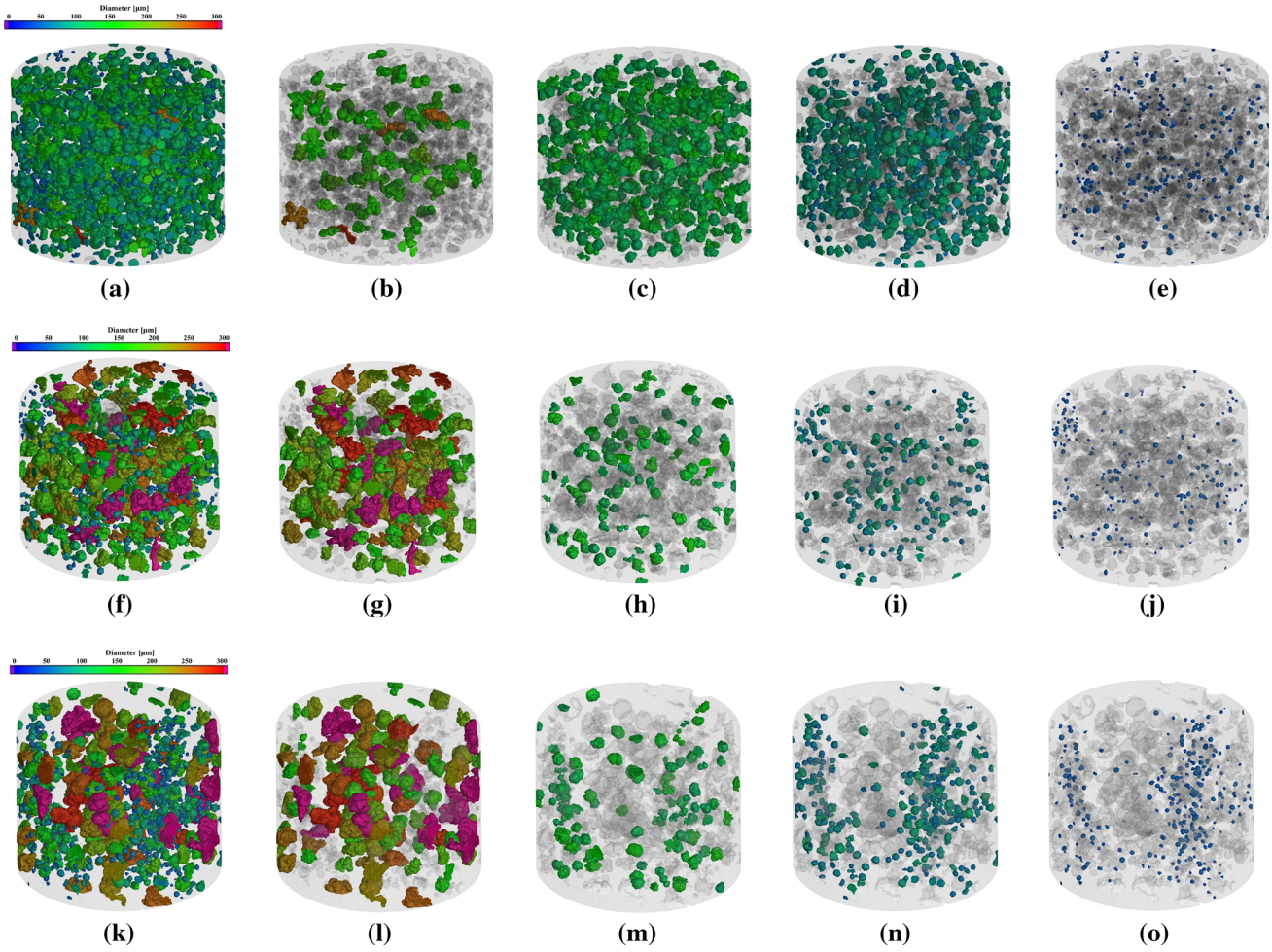

Fig. 5—Spatial distribution of nodules: (*a–e*) are, respectively, graphite nodules distribution of all nodules, nodules larger than 150 μm, nodules with a diameter of 100 to 150 μm, nodules with a diameter of 50 to 100 μm, nodules with a diameter of 25 to 50 μm in sample 0; (*f–j*) are the same in sample 2; (*k–o*) are the same in sample 4. Each 3D volume is $\phi 1.6 \times 1.2$ mm.

smaller than 200 μm; nevertheless, this result is reversed when the diameter is larger than 200 μm in sample 4 because the majority of nodules with sphericity smaller than 0.4 is smaller than 200 μm in sample 4 instead of larger than 200 μm in sample 2.

D. *Metallography*

Although spatial distribution of nodules can be obtained conveniently by X-ray microtomography, it is difficult to acquire the 2D and 3D solidification microstructure morphology of DCI at the same time. In Fe-C-Si alloys, silicon is a kind of negative segregation element. The content of Si in austenite formed early is higher than the content of Si in austenite formed later during the solidification process. According to the classic theory, the distribution of Si can reflect morphology of solidification microstructure.[25,28,29] Hot alkali etching in all three cylindrical rods has been used to display the relationship between graphite nodule distribution and solidification microstructure morphology. The position of metallography is shown in Figure 9. It is shown that the blue/green area is in eutectic cells and that the yellow/brown area is the zone between eutectic cells in Figure 10. By contrasting graphite distribution with solidification microstructure morphology, large nodules are mainly distributed in eutectic cells and the small ones are located between the eutectic cells.

IV. DISCUSSION

A. *Large Graphite Nodules and Small Nodules*

The process of DCI solidification is a typical divorced eutectic solidification, where the nucleation of graphite and austenite are independent. When the temperature of melt decreases to lower than eutectic temperature, the graphite nodules nucleate on small inclusions such as magnesium oxides and sulphides[30] and austenite nucleates in melt independently. As the eutectic reaction continues, the graphite nodules including primary and eutectic graphite will be enveloped by austenite quickly and the growth of graphite is through carbon diffusion in the austenite shell instead of in the melt. So the nodules enveloped by austenite mainly belong to

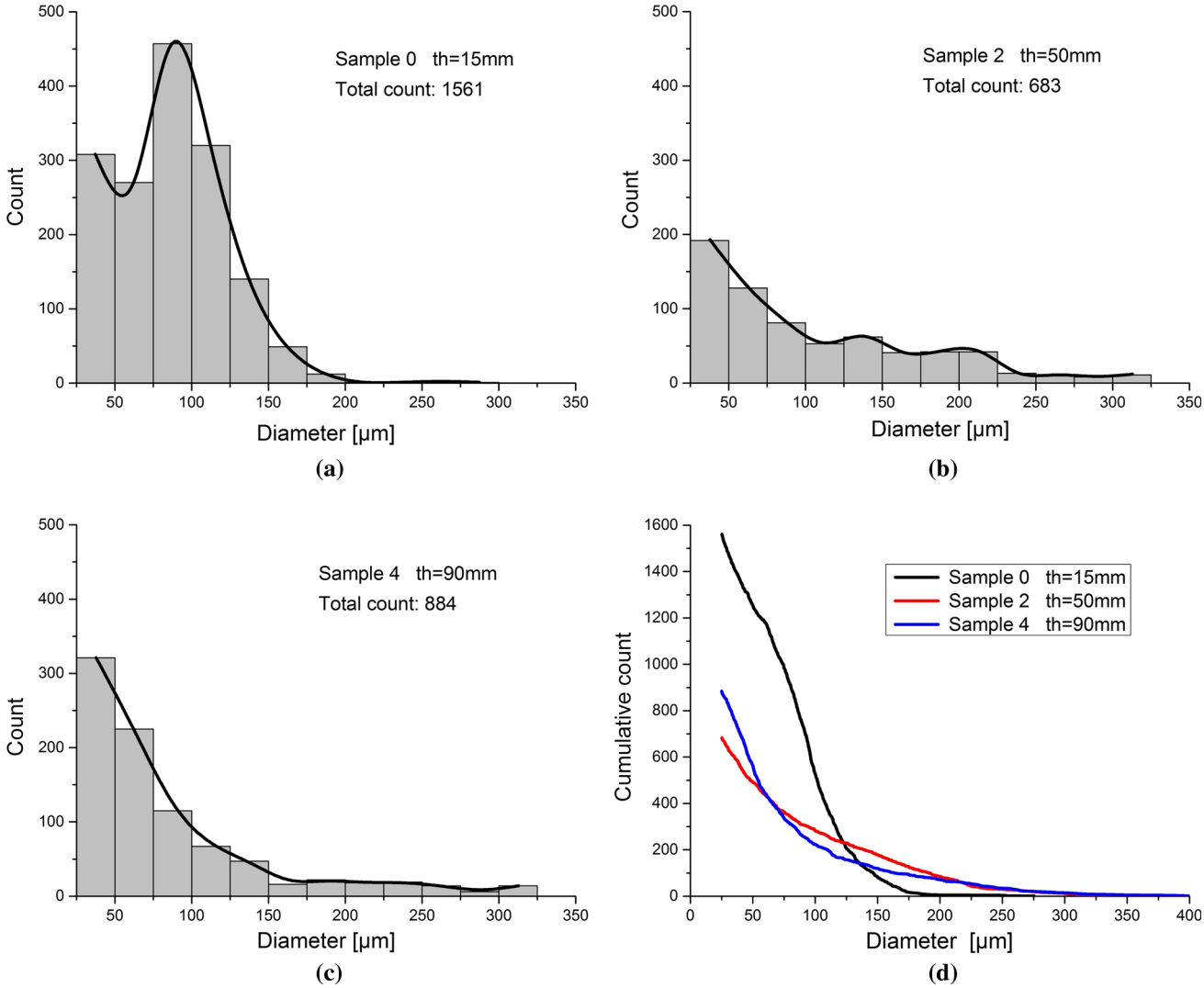

Fig. 6—Nodule diameter and count distribution.

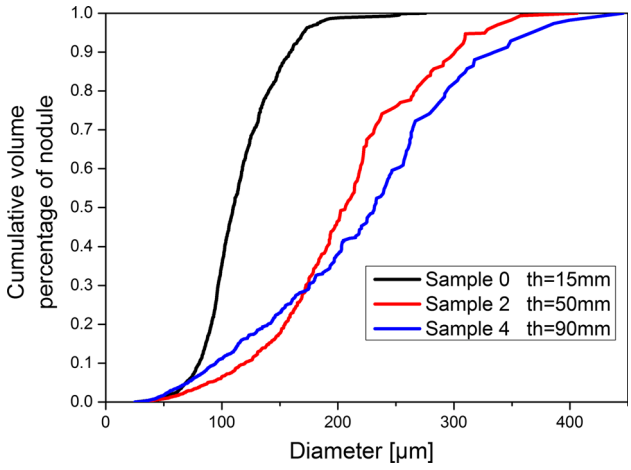

Fig. 7—Nodule diameter and volume distribution.

primary and eutectic graphite. These nodules are distributed uniformly in the matrix as a result of the randomness of the nucleation location and will grow larger because of a long growth time. In Figures 5 and 10, the large nodules are distributed in eutectic cells, especially for a nodule lager than 150 μm in samples 2 and 4.

In the final eutectic stage, the austenite shell gradually grows to a large size, and the liquid between eutectic cells becomes less and less. And the remaining liquid forms "LTF" regions,[31] as shown in the yellow or brown zone in Figure 10. In the LTF regions, there may exist distorted or spherical graphite, inclusion, and shrinkage porosity.[18,31,32] The microstructure forming in this region also results from the cooling rate, chemical composition, and metallurgical nucleation condition. As shown in Figure 10, we can easily find there is no shrinkage porosity, and some tiny inclusions that are mainly smaller than 25 μm are located in the LTF region. So the particles located between eutectic cells are mostly graphite nodules and partially distorted graphite. Therefore, the nodules having a diameter of less than 25 μm are excluded from the nodule count as described in Section II, which can void the interference of inclusion and microporosity.

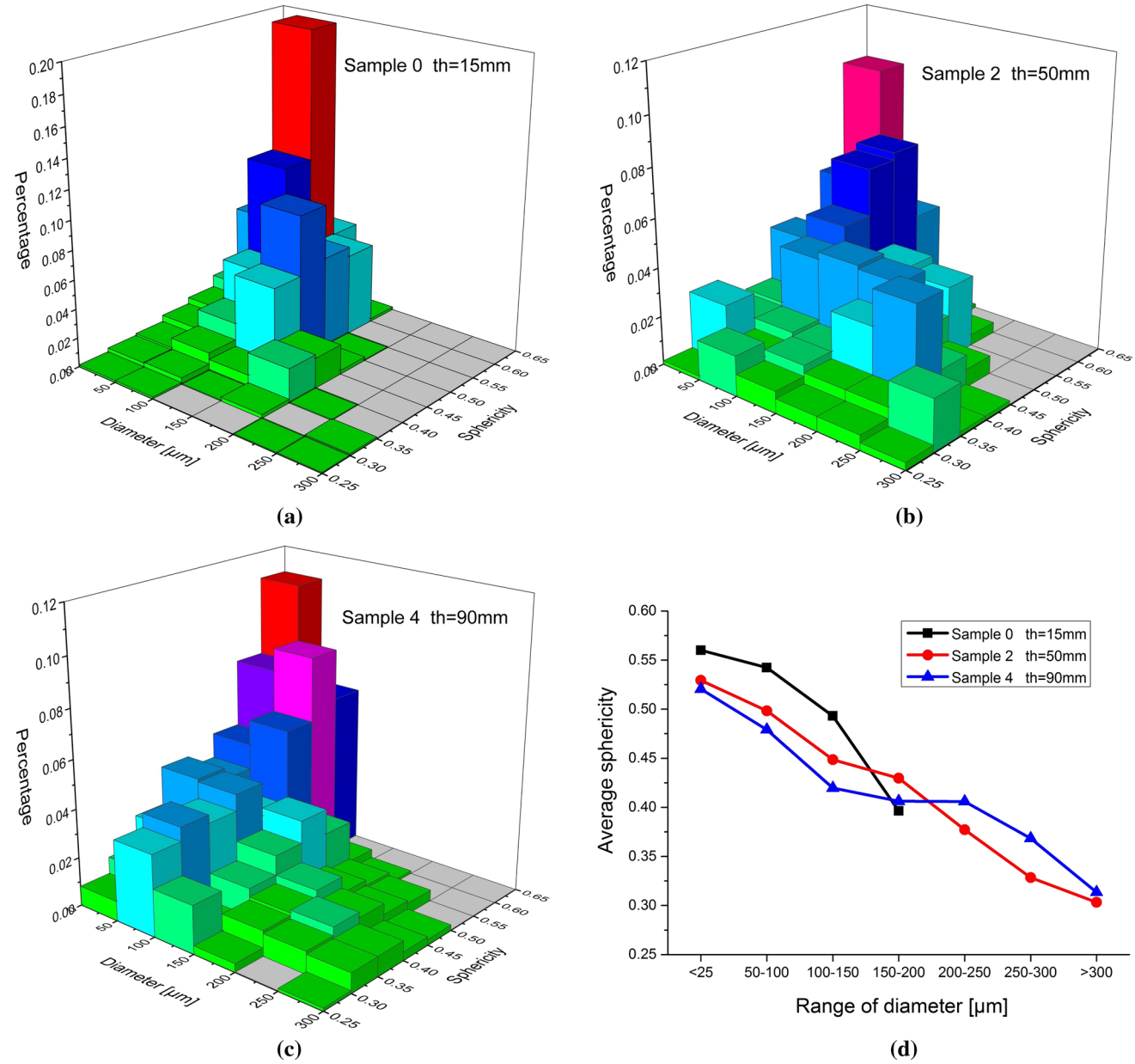

Fig. 8—Nodule sphericity distribution.

B. *Relationship Among Count, Diameter, and Sphericity*

As described, the nodules can be categorized into two categories according to the location of nodules, which are NIECs and NBECs. And NIECs are generally larger than NBECs in a certain thickness casting. So nodules can be artificially categorized according to nodule spatial distribution and diameter. If the nodules within a certain diameter range are distributed uniformly, they are categorized into NIECs. Otherwise, they belong to NBECs. The result is shown in Table III. In sample 0, all nodules are almost distributed in eutectic cells uniformly so they all belong to NIECs. Nodules larger than 100 μm in sample 2 and nodules larger than 150 μm in sample 4 are categorized into NIECs; the rest belong to NBECs. It should be noted that the nodules with a diameter of 50 through 100 μm aggregate more slightly than the nodule with a diameter smaller than 50 μm in sample 2, and the nodules with a diameter of 100 through 150 μm also aggregate more slightly than the nodule with a diameter smaller than 100 μm in sample 4. So part of the nodules with a diameter of 50 through 100 μm in sample 2 and part of the nodules with a diameter of 100 through 150 μm are located in eutectic cells. Nonetheless, they are categorized into NBECs as a result of the difficulty of distinguishing the two kinds of nodules clearly, and a similar qualitative result will be acquired even if they are categorized into NIECs. Thus, the category in Table III is reasonable.

From Table III, it is clear that the count of NIECs decreases and the count of NBECs increases as thickness increases. And most nodules gradually become NBECs instead of NIECs. The count of NIECs is influenced by

T_{eu}. The nucleation rate increases with a decrease in T_{eu}.[33] And T_{eu} decreases as thickness increases according to Table II. So the count of NIECs decreases gradually. On the other hand, the count of NBECs is affected by solute enrichment in LTF regions.[34] Large thickness results in a long solidification time, large LTF region, and serious magnitude of segregation such as Mg, which is a benefit to forming NBECs. So the count of NBECs increases as thickness increases. According to Figure 7 and Table III, although the NIECs account for the minority of total count, they account for the majority of volume as a result of a large diameter in samples 2 and 4.

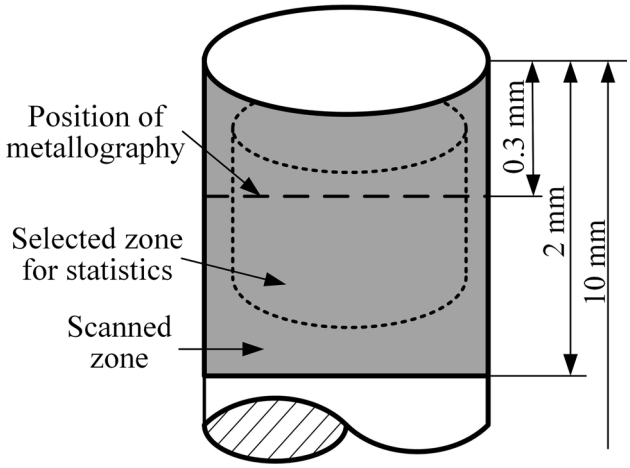

Fig. 9—Sketch of the position of metallography.

The diameter distribution of sample 0 in this study is similar to the study by Tiedje *et al.*[18] if we take the nodules smaller than 25 μm into consideration. Because the plate thickness of sample is 15 mm and the nodules in eutectic are more than that in samples 2 and 4, the properties of diameter distribution are similar to the properties of thin-wall casting. In samples 2 and 4, the count in every diameter interval decreases with an increase of diameter, which is different from the study by Tiedje.[18] It is a result of the effect of NBECs. So the diameter distribution in both sample 2 and sample 4 is a typical distribution in heavy-section casting.

The sphericity is affected by growth type.[20,31] The graphite growth is mainly through carbon diffusion in the liquid before the formation of an austenite shell. After enveloped by austenite, the growth of the graphite nodule is accomplished by carbon diffusion through the austenite shell. If the graphite nodule is partially enveloped in austenite and contact with liquid, the

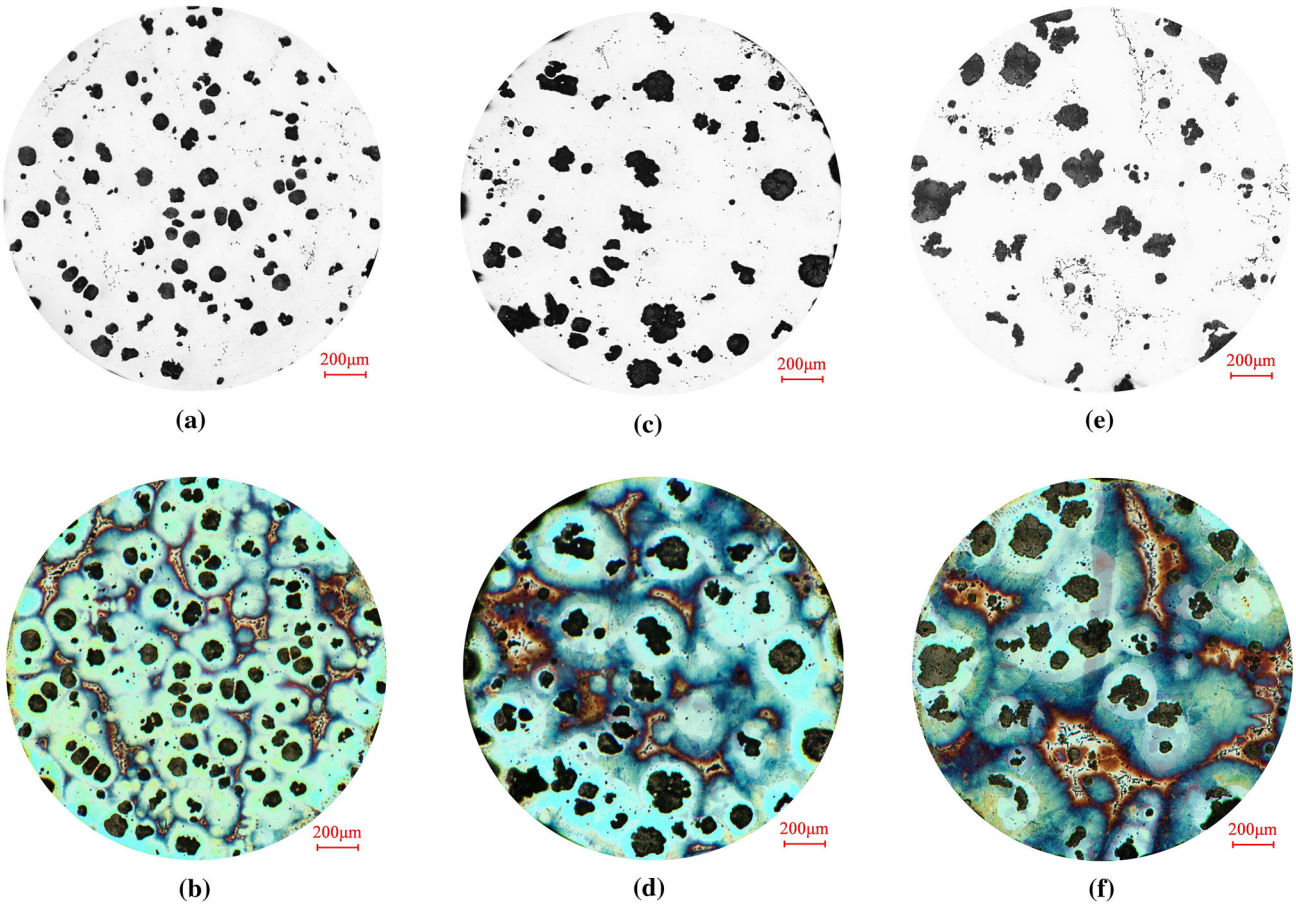

Fig. 10—Microstructure in sample: (*a*, *b*) are graphite nodule distribution in 2D and solidification structure etched by the coloration etchant in sample 0; (*c*, *d*) are the same in sample 2; (*e*, *f*) are the same in sample 4.

Table III. Nodule Categories

Sample Number	NIECs				NBECs			
	Diameter (μm)	Count	Average Sphericity	Volume Percentage (Pct)	Diameter (μm)	Count	Average Sphericity	Volume Percentage (Pct)
0	—	1561	0.52	100.0	—	—	—	—
2	>100	282	0.42	94.0	≤100	401	0.51	6
4	>150	119	0.39	77.0	≤150	765	0.49	33

quasi-spherical graphite nodule will deteriorate into tadpole-shaped or vermicular as a result of the unequal growth velocity. And the probability of the graphite nodule enveloped by austenite increases as the solidification time increases. As a result, the sphericity of NIECs decreases as the thickness increases, as shown in Table III. Meanwhile, if a graphite nodule nucleates earlier, the probability of deterioration increases. So the sphericity decreases as the thickness increases and the sphericity of NIECs is smaller than that of NBECs, as shown in Figure 8(d). It is noted that the quantity of little nodules with low sphericity in sample 4 is bigger than that in sample 2 because of the longer solidification time of the LTF region in sample 4.

The characteristic temperature on cooling curves, T_{eu} and ΔT, can also reflect the change of sphericity. In all three samples, the sphericity of NIECs declines with T_{eu} increasing, which is in accordance with what Fan[35] has found in his research. But the relation between sphericity of NIECs and ΔT in the current study is not agreement with the study by Fan and Stefanescu.[35,36] This may result because of a lack of enough data or other reasons.

C. *Spatial Distribution of Graphite Nodule*

The size of eutectic cells and LTF regions increases with thickness increasing, as shown in Figure 10. When comparing nodule spatial distribution with metallography, the magnitude of nodule agglomeration is in accordance with the size of eutectic cells and LTF regions. As described in Section IV-A, the small graphite nodules are mostly located between eutectic cells. So in Figure 5, the small graphite nodules aggregate between eutectic cells and the large nodules are uniformly distributed in eutectic cells although the 3D solidification microstructure morphology cannot be shown directly. The size of LTF regions increases as thickness increases.[37] Because of the long solidification time, segregation elements have a longer time to diffuse to LTF, resulting in larger segregation coefficients. The positive segregation elements such as Mg are enriched in LTF regions. Locally, a high Mg content in LTF regions results in small graphite nodules.[34] From Table III, it is obvious that the count of NBECs increases with thickness increasing. So the tendency of nodule aggregation is more obvious as thickness increases. The size of the LTF region can also affect the size of nodules located in the LTF region. Because a large LTF region results from a long solidification time, the small nodules have a long time to grow. Nodules with a diameter of 25 to 50 μm aggregate remarkably in sample 2, and the same phenomenon can be found in nodules with a diameter of 50 to 100 μm for sample 4.

Besides the small nodules forming in LTF regions, the lack of small NIECs can also exacerbate the magnitude of nodule aggregation. As shown in Figure 5, there are a few nodules with a diameter of 25 to 50 μm in sample 2 and with a diameter of 25 to 100 μm in sample 4 located in the eutectic cells. On the one hand, NIECs nucleate at the beginning of a eutectic reaction and can grow up fully at the eutectic stage. On the other hand, it may be possible that the larger nodules grow at the expense of small graphite nodules by Ostwald ripening,[38] particularly once the graphite nodules are enveloped by the same continuous austenite matrix. Once this happens, the small graphite nodules will disappear as a result of the small curvature radius and the large nodules will grow up continuously. And this process leads to the phenomenon that there are few small NIECs especially for a heavy section such as sample 4.

V. CONCLUSION

The spatial distribution, count, size, and sphericity distribution of graphite nodules in three dimensions have been quantitatively analyzed in a step-shaped casting by X-ray microtomography and color metallographic techniques. A perfect insight is provided into the morphology of graphite nodules in DCI. The following conclusions can be drawn:

(1) The nodules in DCI can be categorized into two kinds according to nodule location: nodules located in eutectic cells (NIECs) and nodules located between the eutectic cells (NBECs).
(2) The NIECs possess a larger average diameter but smaller sphericity compared with the NBECs, and the sphericity decreases along with the increasing diameter.
(3) The increasing casting thickness results in an increasing count and percentage of NBECs. In addition, most nodules are NIECs in thin walls instead of NBECs in thick walls. The volume of NIECs occupies most of the nodule volume as a result of the large diameter even though NIECs take a low percentage of count in thick walls.

(4) Nonuniform spatial distribution of graphite nodules resulting from the existence of NBECs has been found. Such phenomenon becomes more obvious with an increase of thickness.

ACKNOWLEDGMENTS

This research was financially supported by a project aided by the National Nature Science Fund Projects of China (No. 51305149), China Postdoctoral Science Foundation (2014M552035), and Special Funding of China Postdoctoral Science Foundation (2015T80795).

REFERENCES

1. R. Elliott: *Cast Iron Technology*, Butterworth and Co., London, 1988.
2. N.S. Tiedje: *Mater. Sci. Tech.*, 2010, vol. 26, pp. 505–14.
3. Y. Tanaka, Z. Yang, and K. Miyamoto: *Mater. Trans.*, 1995, vol. 36, pp. 749–56.
4. V.D. Cocco, F. Iacoviello, A. Rossi, M. Cavallini, and S. Natali: *Fatigue Fract. Eng. M*, 2013, vol. 36, pp. 893–902.
5. N. Shiraki, Y. Usui, and T. Kanno: *Mater. Trans.*, 2016, vol. 57, pp. 379–84.
6. I.G. Chen and D.M. Stefanescu: *AFS Trans.*, 1984, vol. 92, pp. 947–64.
7. P. Zhu and R.W. Smith: *AFS Trans.*, 1995, vol. 103, pp. 601–09.
8. A. Sheikhabdolhossein and M. Nili-Ahmadabadi: *Int. J. Cast Met. Res.*, 2005, vol. 18, pp. 295–300.
9. M.I. Onsøien, Ø. Gundersen, Ø. Grong, and T. Skaland: *Metall. Mater. Trans. A*, 1999, vol. 30A, pp. 1053–68.
10. W. Kapturkiewicz, A. Burbelko, and M. Górny: *ISIJ Int.*, 2014, vol. 54, pp. 288–93.
11. D.M. Stefanescu: *Metall. Mater. Trans. A*, 2007, vol. 38A, pp. 1433–47.
12. F.D. Carazo, P.M. Dardati, and D.J. Celentano: *Metall. Mater. Trans. A*, 2016, vol. 47A, pp. 2625–41.
13. A. Natxiondo, R. Suárez, and J. Sertucha: *Metals*, 2015, vol. 5, pp. 239–55.
14. R.E. Ruxanda, D.M. Stefanescu, and T.S. Piwonka: *AFS Trans.*, 2002, vol. 2, pp. 1131–48.
15. L.A. Morales-Hernández, I.R. Terol-Villalobos, and A. Domínguez-González: *J. Mater. Process. Tech.*, 2010, vol. 210, pp. 335–42.
16. C. Basak and A.K. Sengupta: *Scr Mater.*, 2004, vol. 51, pp. 255–60.
17. K.M. Pedersen and N.S. Tiedje: *Mat. Sci. Eng. A*, 2005, vols. 413–414, pp. 358–62.
18. K.M. Pedersen and N.S. Tiedje: *Mater. Charact.*, 2008, vol. 59, pp. 1111–21.
19. S.N. Lekakh, J. Qing, V.L. Richards, and K.D. Peaslee: 117th *Metalcasting Congress*, 2013.
20. D.M. Stefanescu, G. Alonso, and P. Larrañaga: *Acta Mater.*, 2016, vol. 103, pp. 103–14.
21. A. Velichko and F. Cklich: *Int. J. Mater. Res.*, 2009, vol. 100, pp. 1031–37.
22. A. Velichko, C. Holzapfel, and A. Siefers: *Acta Mater.*, 2008, vol. 56, pp. 1981–90.
23. J. Li, L. Lu, and M.O. Lai: *Mater. Charact.*, 2000, vol. 45, pp. 83–88.
24. C. Chuang, D. Singh, and P. Kenesei: *Scr Mater.*, 2015, vol. 106, pp. 5–8.
25. J.Y. Zhou: *China Foundry*, 2009, vol. 6, pp. 152–57.
26. C.F. Yeung, H. Zhao, and W.B. Lee: *Mater. Charact.*, 1998, vol. 40, pp. 201–08.
27. C. Chuang, D. Singh, P. Kenesei, J. Almer, J. Hryn, and R. Huff: *Mater. Charact.*, 2016, DOI:10.1016/j.matchar.2016.08.007.
28. S. Vazehrad, J. Elfsberg, and A. Diószegi: *Mater. Charact.*, 2015, vol. 104, pp. 132–38.
29. K.M. Pedersen, J.H. Hattel, and N.S. Tiedje: *Acta Mater.*, 2006, vol. 54, pp. 5103–14.
30. T. Skaland, Ø. Grong, and T. Grong: *Metall. Mater. Trans. A*, 1993, vol. 24A, pp. 2321–45.
31. J.Y. Zhou: *China Foundry*, 2010, vol. 7, pp. 183–98.
32. D.M. Stefanescu, H.Q. Qiu, and C.H. Chen: *AFS Trans.*, 1995, vol. 103, pp. 189–97.
33. W. Kurz and D.J. Fisher: *Fundamentals of Solidification*, Trans Tech Publications, Aedermannsdorf, 1989.
34. J.Y. Zhou: *China Foundry*, 2010, vol. 7, pp. 292–307.
35. J.H. Fan, F. Chen, and S.G. Zhu: *Foundry*, 2013, vol. 62, pp. 21–24.
36. D.M. Stefanescu, C.R. Loper, R.C. Voigt, and I.G. Chen: *AFS Trans.*, 1982, vol. 90, pp. 333–48.
37. K.L. Hayrynen, G.P. Faubert, and D.J. Moore: *AFS Trans.*, 1989, vol. 97, pp. 747–56.
38. J. Qing, V.L. Richards, and D.C. Van Aken: *Metall. Mater. Trans. A.*, 2016, vol. 47A, pp. 6197–13.